

Discrete effects in stellar feedback: Individual Supernovae, Hypernovae, and IMF Sampling in Dwarf Galaxies

Kung-Yi Su,^{1*} Philip F. Hopkins,¹ Christopher C. Hayward,^{2,3} Xiangcheng Ma,¹ Michael Boylan-Kolchin,⁴ Daniel Kasen,^{5,6} Dušan Kereš,⁷ Claude-André Faucher-Giguère,⁸ Matthew E. Orr¹ and Coral Wheeler¹

¹TAPIR 350-17, California Institute of Technology, 1200 E. California Boulevard, Pasadena, CA 91125, USA

²Center for Computational Astrophysics, Flatiron Institute, 162 Fifth Avenue, New York, NY 10010, USA

³Harvard-Smithsonian Center for Astrophysics, 60 Garden Street, Cambridge, MA 02138, USA

⁴Department of Astronomy, The University of Texas at Austin, 2515 Speedway, Stop C1400, Austin, TX 78712, USA

⁵Department of Astronomy and Theoretical Astrophysics Center, University of California Berkeley, Berkeley, CA 94720, USA

⁶Lawrence Berkeley National Laboratory, 1 Cyclotron Road, Berkeley, CA 94720, USA

⁷Department of Physics, Center for Astrophysics and Space Sciences, University of California at San Diego, 9500 Gilman Drive, La Jolla, CA 92093, USA

⁸Department of Physics and Astronomy and CIERA, Northwestern University, 2145 Sheridan Road, Evanston, IL 60208, USA

Accepted 2018 July 17. Received 2018 July 2; in original form 2017 December 6

ABSTRACT

Using high-resolution simulations from the FIRE-2 (Feedback In Realistic Environments) project, we study the effects of discreteness in stellar feedback processes on the evolution of galaxies and the properties of the interstellar medium (ISM). We specifically consider the discretization of supernovae (SNe), including hypernovae (HNe), and sampling the initial mass function (IMF). We study these processes in cosmological simulations of dwarf galaxies with $z = 0$ stellar masses $M_* \sim 10^4 - 3 \times 10^6 M_\odot$ (halo masses $\sim 10^9 - 10^{10} M_\odot$). We show that the discrete nature of individual SNe (as opposed to a model in which their energy/momentum deposition is continuous overtime, similar to stellar winds) is crucial in generating a reasonable ISM structure and galactic winds and in regulating dwarf stellar masses. However, once SNe are discretized, accounting for the effects of IMF sampling on continuous mechanisms such as radiative feedback and stellar mass-loss (as opposed to adopting IMF-averaged rates) has weak effects on galaxy-scale properties. We also consider the effects of rare HNe events with energies $\sim 10^{53}$ erg. The effects of HNe are similar to the effects of clustered explosions of SNe – which are already captured in our default simulation setup – and do not quench star formation (provided that the HNe do not dominate the total SNe energy budget), which suggests that HNe yield products should be observable in ultra-faint dwarfs today.

Key words: methods: numerical – supernovae: general – ISM: jets and outflows – ISM: structure – galaxies: star formation – cosmology: theory.

1 INTRODUCTION

Stellar feedback is crucial in galaxy evolution. In cosmological simulations without feedback, gas cools rapidly on to galaxies, leading to runaway collapse and star formation, and stellar masses orders of magnitude larger than observed (Katz, Weinberg & Hernquist 1996; Somerville & Primack 1999; Cole et al. 2000; Springel & Hernquist 2003; Kereš et al. 2009 and references therein).

Rapid progress has been made in the last decade in modelling stellar feedback in galaxy simulations (see e.g. Governato et al.

2007; Ceverino & Klypin 2009; Hopkins, Quataert & Murray 2011, 2012c,a; Uhlir et al. 2012; Agertz & Kravtsov 2015). In Hopkins et al. (2011, 2012c), for example, a detailed feedback model including radiation pressure, stellar winds, supernovae (SNe), and photoheating was developed and applied to idealized isolated galaxy simulations. It was shown that this stellar feedback model was able to maintain a self-regulated multiphase interstellar medium (ISM), with giant molecular clouds (GMCs) turning only a few per cent of their mass into stars in a dynamical time, and star formation rate (SFRs) in agreement with observations (Hopkins, Quataert & Murray 2012b; Hopkins et al. 2013a,b). Other groups that implement stellar feedback and explicitly follow molecular hydrogen also see a similar regulation of star formation efficiencies (Hu et al. 2015,

* E-mail: ksu@caltech.edu

2017; Richings & Schaye 2016). With numerical improvements and additional cooling physics, similar models were applied to cosmological zoom-in simulations in the FIRE¹ (Feedback In Realistic Environments) project (Hopkins et al. 2014). Subsequent work showed these feedback models could reproduce a wide range of observations, including star formation histories (Hopkins et al. 2014), the Kennicutt–Schmidt relation (Orr et al. 2017), the star-forming ‘main sequence’ and time-variability of star formation (Sparre et al. 2017), galactic winds (e.g. Muratov et al. 2015, 2017; Anglés-Alcázar et al. 2017), the dense H I content of galaxy haloes (Faucher-Giguère et al. 2015, 2016; Hafen et al. 2017), the implied photon escape fractions of high-redshift galaxies (Ma et al. 2016), and galaxy metallicities (Ma et al. 2015a).

However, there are several properties of discrete feedback processes that without proper modelling could potentially yield very different or even unreasonable ISM phase structures and galaxy morphologies. SNe are very effective at regulating the SFR (e.g. Kim, Ostriker & Kim 2013, 2014; Kim & Ostriker 2017), and they are naturally discrete events and tend to be clustered in time and space. Idealized studies of the ISM have shown that if the same total amount of energy is injected continuously into the ISM rather than in discrete SNe (or at too low resolution), the energy could be effectively smeared throughout the whole galaxy and be radiated away too efficiently (Kim & Ostriker 2015; Martizzi, Faucher-Giguère & Quataert 2015; Martizzi et al. 2016), thus making SNe feedback much less effective than when the spatiotemporal clustering of SNe is properly modelled (e.g. Girichidis et al. 2016b; Fielding et al. 2017). In many simulations (including those referenced above), SNe are indeed correctly treated as individual discrete events, but this is not always the case in the literature. The effects of the discreteness and clustering of SNe are explicitly studied in high-resolution simulations of ISM gas with various densities in Kim, Ostriker & Raileanu (2017). It is shown that how clustered SNe can affect the evolution of the resulting superbubbles and the effective radial momentum per SN event. It is therefore interesting to see how this would affect galaxy-scale simulations.

Moreover, it is common in galaxy-scale simulations to treat continuous quantities (e.g. stellar mass-loss and radiative heating rates) as initial mass function (IMF)-averaged. In reality, these rates are highly variable star-to-star, with most of the feedback from OB-winds, ionizing photons, and radiation pressure coming from massive O stars. When galaxies are sufficiently massive, these effects should average out, but in dwarfs, in particular, failure to account for these fluctuations could lead to biased predictions for galaxy properties. This is certainly the case for measurements of e.g. the ionizing flux and spectral shapes of such systems (see da Silva, Fumagalli & Krumholz 2012; Krumholz et al. 2015). IMF sampling gets more important when the mass resolution increases, and the baryonic particle mass fall below $\sim 10^4 M_\odot$ (Hensler, Steyrleithner & Recchi 2017; Hu et al. 2017). In such case, the IMF is poorly sampled in a single star particle.

In addition to the aforementioned effects, hypernovae (HNe) may be yet another important discrete feedback channel. HNe are core-collapse SNe that have energies that exceed the typical SN energy ($\sim 10^{51}$ erg) by a factor of 10 or more ($E > 10^{52}$ erg; Nomoto et al. 2004; Podsiadlowski et al. 2004). Such extreme events could potentially blow out all the gas in a dwarf galaxy, consequently completely quenching star formation if the galaxy’s dark matter halo is too low mass to accrete further gas post-reionization. Whether

or not HNe quench star formation determines whether its yield products can be incorporated into next-generation stars, which in turn determines whether or not the yield products of HNe should be observable.

In this paper, we investigate the effects of the discretization of SNe, IMF sampling, and the inclusion of HNe on the formation of dwarf galaxies. In Section 2, we describe the simulations. Then, we analyse the effects on the star formation histories, morphologies, phase structures, outflows, and ionizing photon escape fractions of our simulated galaxies in Section 3. In Section 4, we discuss our results, and our conclusions are presented in Section 5.

2 METHODOLOGY

The simulations use GIZMO (Hopkins 2015),² a mesh-free, Lagrangian finite-volume Godunov-type code designed to capture both the advantages of grid-based and smoothed-particle hydrodynamics methods, in its meshless finite mass mode. The numerical details and tests of the method are discussed in Hopkins (2015). The default simulations use the FIRE-2 version of the code, which is described in detail in Hopkins et al. (2018b). Cooling is followed from $10-10^{10}$ K, including free-free, inverse Compton, atomic, and molecular cooling, accounting for photoionization and photoelectric heating by a ultraviolet (UV) background (Faucher-Giguère et al. 2009) and local sources.³ Star formation occurs only in molecular, self-shielding, and self-gravitating (Hopkins, Narayanan & Murray 2013c) gas above a minimum density $n > 1000 \text{ cm}^{-3}$.

We focus on low-mass dwarf galaxies, where the effects we explore should be more significant than in more massive galaxies. Three fully cosmological zoom-in simulations from the FIRE-2 suite (Hopkins et al. 2018b) are included in this study: m10q (an early-forming $10^{10} M_\odot$ halo), m10v (a late-forming $10^{10} M_\odot$ halo), and m09 (a $10^9 M_\odot$ halo). Note that the tabulated halo masses are from $z = 0$.

The initial conditions of the runs are listed in Table 1. Most of the simulations have been re-run at different resolutions, with the initial gas particle masses differing by a factor of ~ 100 . We find all of the conclusions of this paper are insensitive to mass resolution. A resolution test can be found in Appendix A. For all runs, a flat Λ CDM cosmology with $h = 0.702$, $\Omega_M = 1 - \Omega_\Lambda = 0.27$, and $\Omega_b = 0.046$ is adopted.

For each galaxy, we consider four variations of the stellar feedback implementation in the simulations:

(i) **Default FIRE-2 Feedback Physics (‘Default’)**: This is our standard FIRE-2 implementation (Hopkins et al. 2018b). To summarize: once formed, a star particle is treated as a single-age stellar population with metallicity inherited from its parent gas particle and age appropriate for its formation time. All corresponding stellar feedback inputs (SNe and mass-loss rates, spectra, etc.) are de-

²A public version of this code is available at <http://www.tapir.caltech.edu/~phopkins/Site/GIZMO.html>.

³Since this paper was submitted, we identified an error in the treatment of heating by CR backgrounds (usually only important in very dense, star-forming gas) that artificially enhances the IGM temperature at very high redshifts $z \sim 100$ (it has no effect after re-ionization begins). This leads to some artificial suppression of star formation in our smallest galaxies (m09 and m10v) at $z \gg 10$. However, since it affects all runs in the same way, and we do not include any ‘first stars’ model in the first place to properly capture the behaviour at these redshifts, our conclusions in this paper should be unaffected.

¹Project web site: <http://fire.northwestern.edu>

Table 1. Galaxy simulations.

Simulation Name	$M_{\text{halo}}^{\text{vir}}$ (M_{\odot})	R_{vir} (kpc)	M_{g} (M_{\odot})	$M_{\text{*}}$ (M_{\odot})	$m_{i,1000}$ ($1000M_{\odot}$)	$\epsilon_{\text{gas}}^{\text{min}}$ (pc)	Description
m10q	8.0e9	52.4	8.4e6	1.8e6	0.25	0.52	Isolated dwarf, early-forming halo
m10v	8.3e9	53.1	2.1e7	1.0e5	0.25	0.73	Isolated dwarf, late-forming halo
m09	2.4e9	35.6	1.2e5	9.4e3	0.25	1.1	Early-forming, ultra-faint field dwarf

Notes: Parameters of the galaxy models studied here:

- (1) Simulation name: Consistent with Hopkins et al. (G2018b).
- (2) $M_{\text{halo}}^{\text{vir}}$: Virial mass (Bryan & Norman 1998) of the main halo at $z = 0$.
- (3) R_{vir} : Virial radius of the main halo at $z = 0$.
- (4) M_{g} : Total gas mass within $\sim 0.1R_{\text{vir}}$ at $z = 0$ ($z = 2$ for m09).
- (5) $M_{\text{*}}$: Total stellar mass within $\sim 0.1R_{\text{vir}}$ at $z = 0$.
- (6) $m_{i,1000}$: Baryonic (star and gas) mass resolution in units of $1000 M_{\odot}$. Dark matter particles are always ~ 5 times heavier.
- (7) $\epsilon_{\text{gas}}^{\text{min}}$: Minimum gravitational force softening reached by the gas in the simulation (force softenings are adaptive following the inter-particle separation). Force from a particle is exactly Keplerian at $> 1.95\epsilon_{\text{gas}}$; the 'Plummer-equivalent' softening is $\approx 0.7\epsilon_{\text{gas}}$.

terminated using STARBURST99 (Leitherer et al. 1999) to compute the IMF-averaged rate for a Kroupa (2002) IMF. The stellar feedback model includes the following: (1) radiative feedback in the form of photoionization and photoelectric heating, in addition to single and multiple-scattering radiation pressure with five bands (ionizing, FUV, NUV, optical-NIR, and IR) tracked; (2) stellar mass loss with continuously injected mass, metals, energy, and momentum from OB and AGB winds; (3) SNe Types II and Ia using tabulated SNe rates as a function of stellar age the IMF to determine the probability of an SN originating in the star particle during each time-step⁴ and then determine stochastically whether an SN occurs by drawing from a binomial distribution. If an event occurs, the appropriate gas mass, metal mass, momentum, and energy are injected – in other words, SNe are discrete events. We assume that each SNe has an initial ejecta energy of 10^{51} erg (see Hopkins et al. 2018a,b for details regarding how this is coupled). To separate the effects of IMF sampling and HNe from purely simulation stochastic effects (which vary from simulation to simulation, for the same physics), two m10q simulations are evolved with the same default physics but different random number seeds. They are labelled 'Default' and 'Default 2', respectively.

(ii) **Continuous SNe Energy Injection ('Continuous')**: Here, we take our 'Default' model but modify it by treating SN feedback as a continuous rather than discrete process. Specifically, for each star particle, we take the expectation value for the probability of an SN occurring in a given time-step in a star particle and simply inject that *fraction* of a single SN's feedback-related quantities (e.g. gas mass, metal mass, energy, and momentum).⁵ Thus, the energy in this case is 'smeared' in both time and space, as if SN feedback were continuous (as stellar winds and radiation are). The continuous feedback simulations are not evolved all the way to $z = 0$, as they become very expensive as gas catastrophically collapses into dense structures.

(iii) **(Approximate) IMF-Sampling Effects ('IMF-SMP')**: In this case, we take our 'Default' model and implement a very simple approximation for the effects of discreteness resulting from IMF sampling, particularly for the radiative feedback and stellar mass-loss channels. Since the simulations are still of far too low resolution to actually resolve the IMF and the feedback channels of

interest are completely dominated by massive stars, we implement an intentionally simplified 'toy model' for IMF sampling. Specifically, each time a star particle forms, we determine the number of massive 'O stars', N_{O} , from a Poisson distribution with expectation value $\langle N_{\text{O}} \rangle \approx m_{\text{particle}}/100 M_{\odot}$. All feedback rates that depend on massive stars (photoionization and photoelectric heating, radiation pressure in the UV, OB winds, and core-collapse SNe rates) are then scaled by the 'O-star number', i.e. their IMF-averaged rates are multiplied by $N_{\text{O}}/\langle N_{\text{O}} \rangle$ (so, by definition, the IMF-averaged rates are recovered). In the SNe case, whether an SN event happens is then determined stochastically by drawing from a binomial distribution according to the updated SNe rate. Each time a core-collapse SN occurs, we delete one 'O star'.

(iv) **Hypernovae ('IMF-SMP+HNe')**: Observationally, HNe are rare. One category of events that is referred to as HNe is energetic SNe associated with gamma-ray bursts (broad-lined Type Ic SN). They occur at a rate that is only ~ 5 per cent of the Type Ib/Ic rate, with more energetic events ($E_{\text{HNe}} \gtrsim 10^{52}$ erg) representing roughly ~ 1 per cent of the total core-collapse SNe rate (Podsiadlowski et al. 2004; Soderberg et al. 2006; Guetta & Della Valle 2007). Another class of HNe has been theorized to come from the pair-instability SN from massive stars with 10^{53} erg but $< 10^{-4}$ of the SN rate (Gal-Yam 2012).

Here, we are interested in the most extreme events (which would have the most dramatic effects on their host galaxies), so based on the event rate distribution in Hansen (1999), we assume an HN energy of $E_{\text{HNe}} = 10^{53}$ erg (i.e. $100 \times$ a typical SN) and an event rate that is 10^{-3} times the normal core-collapse SN rate.⁶ In our m10q simulation, we simply assign each core-collapse event a random probability of being an HN equal to 0.1 per cent, and, if the event is defined a HNe, we increase the energy of the ejecta by a factor of 100, but the ejecta mass is kept the same. In our m09 and m10v simulations, the stellar mass is sufficiently low that the expectation value of the number of HNe is $\lesssim 1$, so we take our 'IMF-SMP' runs, re-start them just after one of the peak star formation events (at $z = 0.31$ for m10v and $z = 4.0$ for m09) and manually insert a single HN explosion at that time. Note that these choices ensure that the *total* energy contributed by HNe is only ~ 10 per cent of the SNe budget, so we are not changing the IMF-averaged properties significantly.

⁴For particle masses $\approx 250 M_{\odot}$ and typical time-steps in dense star-forming gas of ~ 100 yr, the probability of an SN in a young (~ 3 – 10 Myr old) star particle in one time-step is $dp \sim 10^{-5}$.

⁵This can be as little as $\sim 10^{46}$ erg per time-step in dense, star-forming gas.

⁶This may be close to an upper limit unless the IMF is more top-heavy.

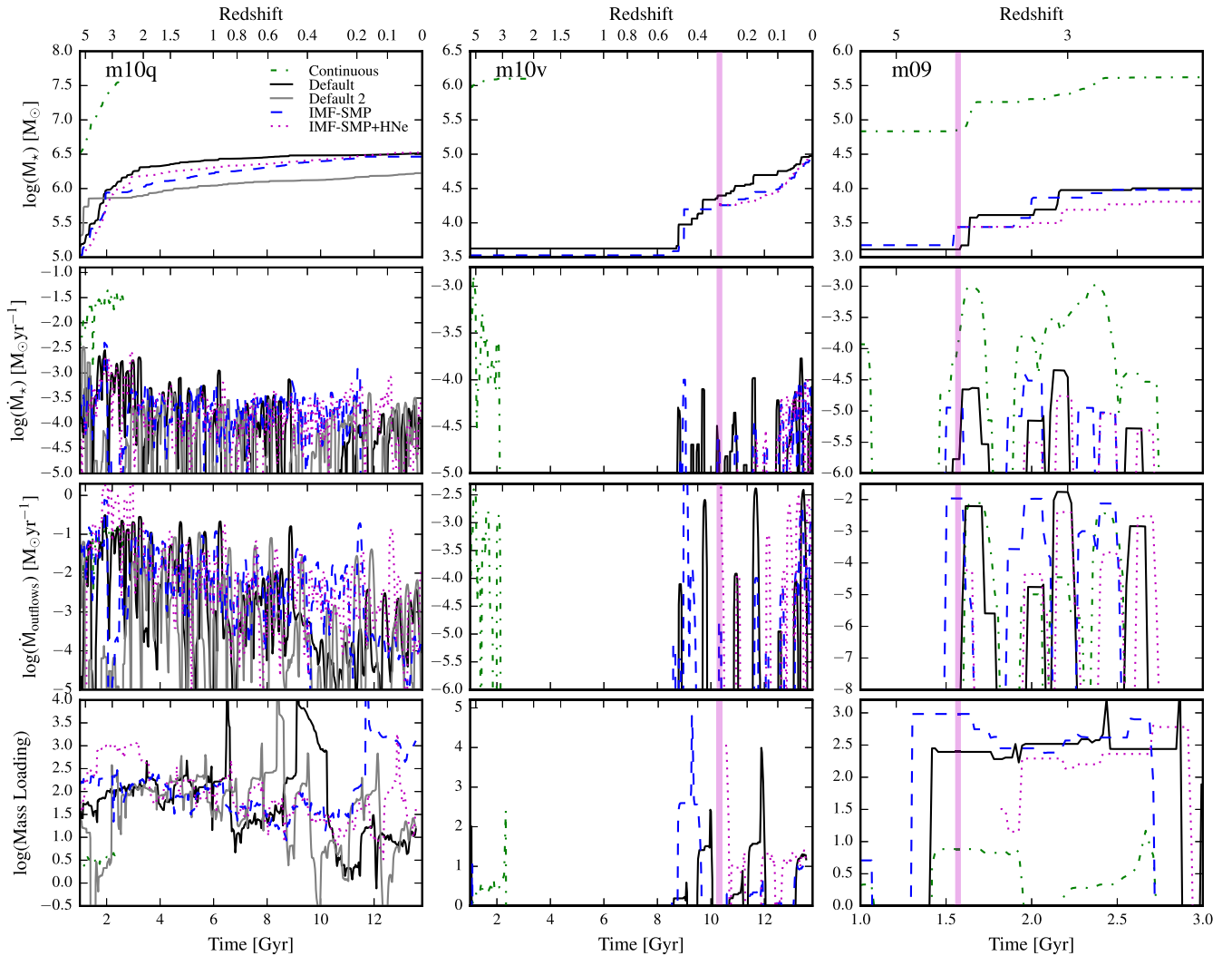


Figure 1. **Top row:** Stellar mass as a function of cosmic time in our simulations. The vertical magenta lines label the times when HNe are manually exploded in the m10v and m09 runs (m10q, being more massive, has ~ 30 HNe randomly distributed among the SNe over its history). **Second row:** SFR averaged over the preceding 100 Myr as a function of time. **Third row:** The mass outflow rate as a function of time smoothed over 100 Myr. To estimate the mass-outflow rate, we consider all gas particles between 0.08 and $0.1 r_{\text{vir}}$ that have radial velocities greater than 30 km s^{-1} . **Bottom row:** Outflow mass-loading factor, $\eta \equiv \dot{M}_{\text{outflow}} / \dot{M}_{\text{SFR}}$, smoothed over 500 Myr. Treating SN feedback as continuous results in higher SFRs – and thus stellar masses – and lower outflow mass loading factors. The final stellar mass of m10q ‘Default’ and ‘Default 2’ runs differs by a factor of ~ 2 . Given such range of stochastic effect, the effect of IMF sampling or HNe is not obvious. In the m09 run in which an HN was included, the final stellar mass is reduced by ~ 0.2 dex. All panels are plotted after the first Gyr of the simulation when the haloes are slightly more settled, and the outflows are more well defined.

3 RESULTS

3.1 Star formation rates

The first two rows of Fig. 1 show the cumulative stellar mass and an SFR averaged in a 100-Myr interval for each galaxy. In all cases, the ‘Continuous’ runs have an order of magnitude greater final stellar mass, indicating that the SN feedback is effectively weaker than in the ‘Default’ model. Although the same amount of SNe energy is deposited into the surrounding gas particles in an integral sense, it is radiated away before doing significant work on the surrounding dense ISM significantly because the feedback is temporally diluted (a manifestation of the well-known overcooling problem in galaxy formation simulations).

On the other hand, IMF sampling does not appear to have a significant systematic effect on stellar masses, i.e. the effects of IMF sampling appear smaller than purely stochastic simulation varia-

tions. The m10q ‘Default’ and ‘Default 2’ runs differ significantly in star formation histories, with final stellar masses differing by a factor of ~ 2 , even though these two runs use exactly the same physics. Two more m10q ‘IMF-SMP’ runs evolved to $z \sim 0.6$ show a similar range of stochastic differences. We thus find that the purely stochastic run-to-run variation with the same physics but with different random number seeds (resulting in variations in the detailed ages and relative positions of star particles, and therefore, the feedback injection sites) is larger than the variation when IMF sampling is included. The difference in SFRs among m10q runs is connected to the variations in gas phase structure and outflows, which will be discussed in Sections 3.2 and 3.3.

In the m10q ‘IMF-SMP’ run, an extreme but apparently stochastic overlap of many SNe at the same time (at $z \sim 0.2$) expels a large fraction of the galaxy’s gas supply, causing a decrease in the SFR for an extended period of time. A similar event can be observed

in the m10q 'IMF-SMP+HNe' run at $z \sim 0.09$, although it is not as dramatic. These events are also a result of stochastic variations instead of differences in the feedback implementations. Of course, the very fact that stochastic effects can be this dramatic in such small dwarfs owes to the fact that just a relatively small number of highly clustered SNe can significantly perturb the galaxy.

After manually exploding HNe in m10v and m09, star formation ceases for only a few million years. HNe do not indefinitely quench star formation even in our smallest halo in this study (m09), nor do they affect the star formation histories in a qualitatively different manner from overlapping SNe events that occur after, e.g. the formation of a modest-size star cluster in a massive GMC. Note that m09 is quenched after reionization, although it takes until $z \sim 3$ for the galaxy to exhaust its existing cold gas supply (see Fitts et al. 2017); this behaviour is the same for all of the m09 runs considered here.

3.2 Phase structure

Figs 2 and 3 quantify the density distribution of gas particles in temperature bins of cold (< 8000 K), warm ($8000\text{--}10^5$ K) and hot ($> 10^5$ K) gas at various epochs. In the m10v case, since the 'IMF-SMP+HNe' run is restarted from the 'IMF-SMP' run at $z = 0.31$ upon exploding a HNe and most of the star formation happens after that, only the low redshift ($z = 0\text{--}0.31$) results are shown. On the other hand, star formation in m09 ceases by $z \sim 2$ and therefore only $z = 2\text{--}4$ results are shown. The phase structure is broadly consistent with dwarf galaxy simulations from other groups (see e.g. Hu et al. 2016, 2017; Richings & Schaye 2016).

Again, the 'Continuous' runs differ from the other runs most dramatically in all cases. All the runs with continuous SNe have higher total gas mass, especially in the cold and warm temperature bins. The total stellar mass is also orders of magnitude higher, which indicates that, without discretizing SNe, feedback is much less efficient and more gas can accrete on to the galaxy.

The lack of cold gas in m10q 'Default 2' run during the $z = 2\text{--}4$ interval is consistent with its lower SFR in the same period. The lower SFR also results in less hot, intermediate density gas. Given the difference between m10q 'Default' and 'Default 2' runs, the effect of IMF sampling on phase structure is not obvious. IMF sampling does not appear to systematically alter the phase structure of the gas in m10v and m09 as well. Since FIRE dwarf galaxies at this mass scale have relatively bursty star formation histories (El-Badry et al. 2016; Faucher-Giguere 2018; Fitts et al. 2017; Sparre et al. 2017), IMF sampling is likely subdominant to bursts in establishing the phase structure of gas in these simulations.

In all cases, HNe do not alter the phase structure significantly. Whenever HNe occur, its effects only last for a few million years.

3.3 Outflows

The third row of Fig. 1 shows the outflow rate as a function of time in the simulations. The value shown is averaged over a 100-Myr period. To isolate 'outflows', we simply take all gas within a thin layer from 0.08 to $0.1 r_{\text{vir}}$ that has an outward radial velocity greater than 30 km s^{-1} (comparable to the circular velocity in these dwarfs). The bottom row of Fig. 1 is the outflow mass-loading, defined as $\dot{M}_{\text{outflow}}/\dot{M}_{\text{SFR}}$, indicating the efficiency of stellar feedback at driving outflows. The plotted mass-loading is averaged over 500 Myr to suppress stochastic effects. The density distributions of the outflows are shown in the fourth columns of Figs 2 and 3.

The 'Continuous' runs again demonstrate fundamental differences: despite having similar outflow masses to the other runs, the star formation rate in the 'Continuous' runs is an order of magnitude higher and the mass-loading is therefore much lower. This indicates that without discretizing SNe, the 'smeared' SNe energy injection is much less efficient at accelerating gas into outflows.

The difference in outflows among the other m10q runs is consistent with the variation in star formation rates as the difference in outflow mass-loading is not significant during most of the time. This suggests that feedback efficiency in each run is similar on the average. Given the stochastic variance we see from the 'Default' and 'Default 2' runs, the effect of IMF sampling is again not obvious.

A peak of outflow can be seen just right after the manually exploded HNe in the m10v and m09 cases. However, the long-term effects of HNe in these runs are, again, not obvious.

3.4 Ionizing photon escape fractions

To investigate the ionizing photon escape fractions, we follow the method in Ma et al. (2015b, 2016). All the snapshots are processed by the 3D Monte Carlo radiative transfer (MCRT) code, basing on SEDONA base (Kasen, Thomas & Nugent 2006). For each snapshot, the intrinsic photon budget Q_{int} is calculated as the sum of the photon budget of each star particle estimated through the BPASSv2 (Stanway, Eldridge & Becker 2016) model, which includes detailed binary evolution effects. Because the model stellar evolution tracks exist only for certain metallicities, the input metallicity is assumed to be $0.001 (0.05 Z_{\odot})$,⁷ which is roughly the averaged value in the simulations. We also assume 40 per cent of the metals are in dust phase with opacity $10^4 \text{ cm}^2 \text{ g}^{-1}$ (Dwek 1998; Fumagalli et al. 2011). In the runs considering the effects of sampling the IMF, the photon budget from each star is scaled properly with its O-star number.

The MCRT code includes photoionization (Verner et al. 1996), collisional ionization (Jefferies 1969), and recombination (Verner & Ferland 1996). We run the calculation iteratively to reach converged results by assuming the gas in ionization equilibrium. The escape fraction is defined as the $Q_{\text{esc}}/Q_{\text{int}}$, where Q_{esc} is the calculated number of escaped photons at approximately R_{vir} . Some examples of convergence test can be found in Ma et al. (2015b).

Fig. 4 shows the 400-Myr averaged escape fraction for m10q and m10v runs. There are very few snapshots with young star particles (< 5 Myr old, when most ionizing photons are emitted) in m09 and in m10v before $z = 0.6$, so the results in those periods are poorly sampled and are therefore not shown. The photon escape fractions are highly variable during the simulated period, ranging from $\lesssim 0.001$ to 0.25 , but no systematic effect from different models is observed.

The effects of IMF sampling on photon escape fractions are small. IMF sampling mainly affects the photon budget when there are O stars in the star particles. However, those stars are mostly deeply buried in dense GMCs from which the photons rarely escape in any case.

4 DISCUSSION

4.1 IMF Sampling effects

We see no obvious effects from our IMF sampling model (in the properties we have analysed). Our implementation of IMF sampling

⁷We use $Z_{\odot} = 0.02$ (Anders & Grevesse 1989).

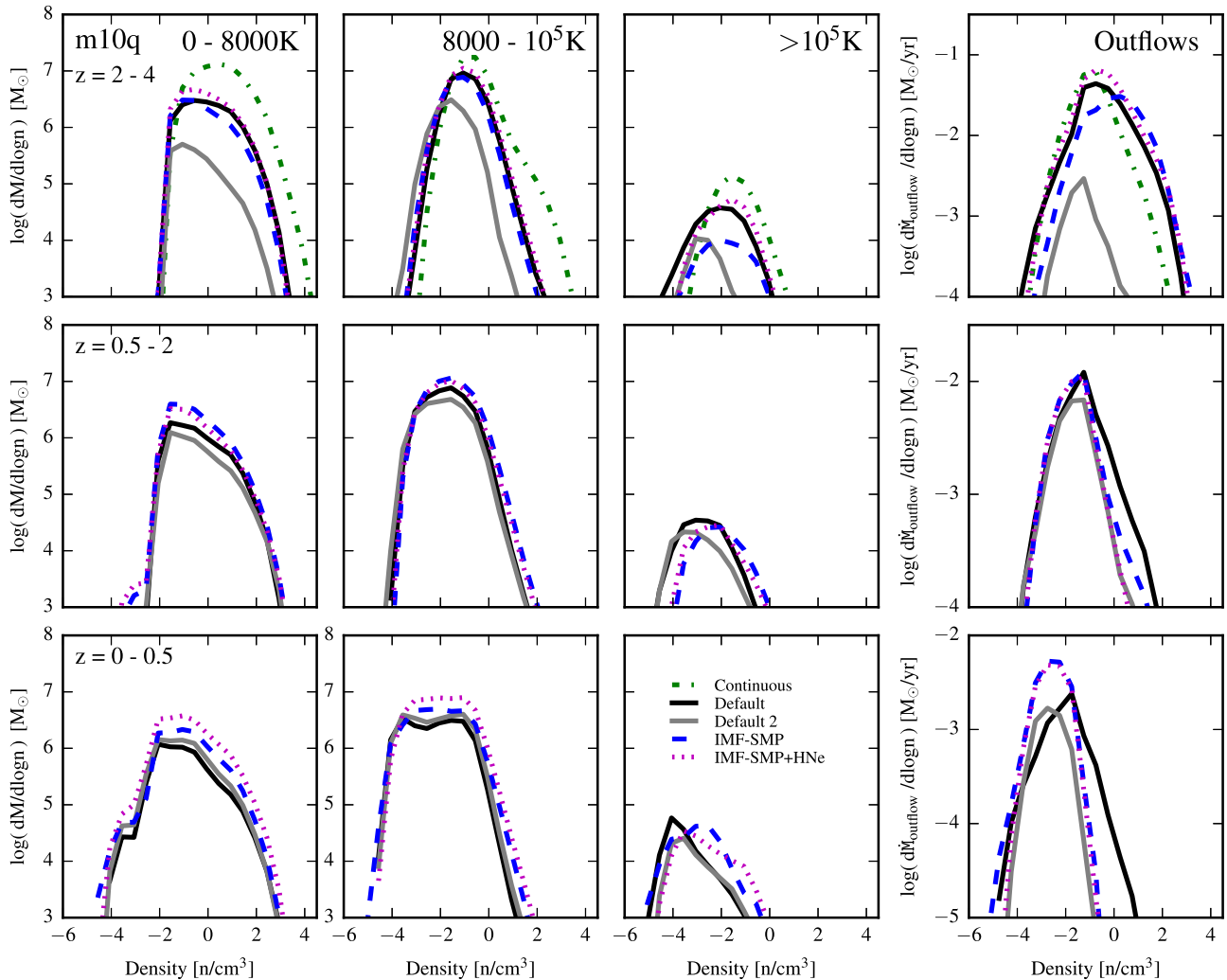


Figure 2. Gas density distributions for m10q. Rows show the properties at different redshifts; columns show phases including cold-neutral (*left*), warm-ionized (*middle left*), hot (*middle right*), and in outflows (*right*). The ‘Continuous’ run has more gas in all temperature bins, owing to less-efficient feedback. Owing to the orders of magnitude higher stellar mass, it produces a significant outflow despite the feedback being effectively weaker. Given the stochastic difference between ‘Default’ and ‘Default 2’ runs, the effect of IMF sampling is not obvious.

is based on a simple scaling of the local magnitude of feedback according to the number of massive O stars. Those GMCs with higher O-star number can be destroyed more easily by feedback (both from SNe and ‘pre-processing’ radiative feedback and OB-winds) and form fewer stars in their lifetime. On the other hand, in the regions (periods) where (when) there are fewer O stars, the effects of feedback are weaker and therefore the gas accretion rate increases.

In larger haloes (e.g. SMC-mass and larger), which form orders of magnitude more stars and have much deeper potential wells, phenomena such as galactic winds result from the collective effects of many stars. Hence, the local variation of O-star number will be less significant.

On the other hand, in the haloes where many fewer stars are formed (e.g. dwarfs such as m09, m10v or m10q), the amount of gas in the close neighbourhood of young stars is reduced, and a single SNe (which is already discretized in these simulations) has a large feedback effect regardless of whether or not other SNe explode nearby. As a result, the spatial and time variation of the local magnitude of feedback is already large, and IMF sampling

may be a secondary effect compared to strong stellar clustering.

It is also worth noting that IMF sampling does not statistically change the spatial and time distribution of SNe events (primarily determined by the distribution of star formation events, which trace the dense, self-gravitating ISM gas), other than linking the strength in each feedback channel to the local O-star number. In other words, it does not on average increase SNe rate, and nor does it make SNe more or less clustered.

In the runs with IMF sampling, the number of O stars is drawn from a Poisson distribution with mean and variance equal to the average number of O stars. Regardless of the random numbers drawn, most O stars will explode as SNe within 30 Myr. As a result, the statistical properties of SNe are roughly the same as with the default physics. An important difference in runs with IMF sampling is that star particles with higher O-star numbers will not only have more SNe but also generate more powerful stellar wind and radiative feedback (instead of IMF-averaged). In other words, the modified SNe feedback is synchronized with the other feedback channels. Although this may further boosts the total feedback strength in different regions beyond merely the variation in SNe, such boost

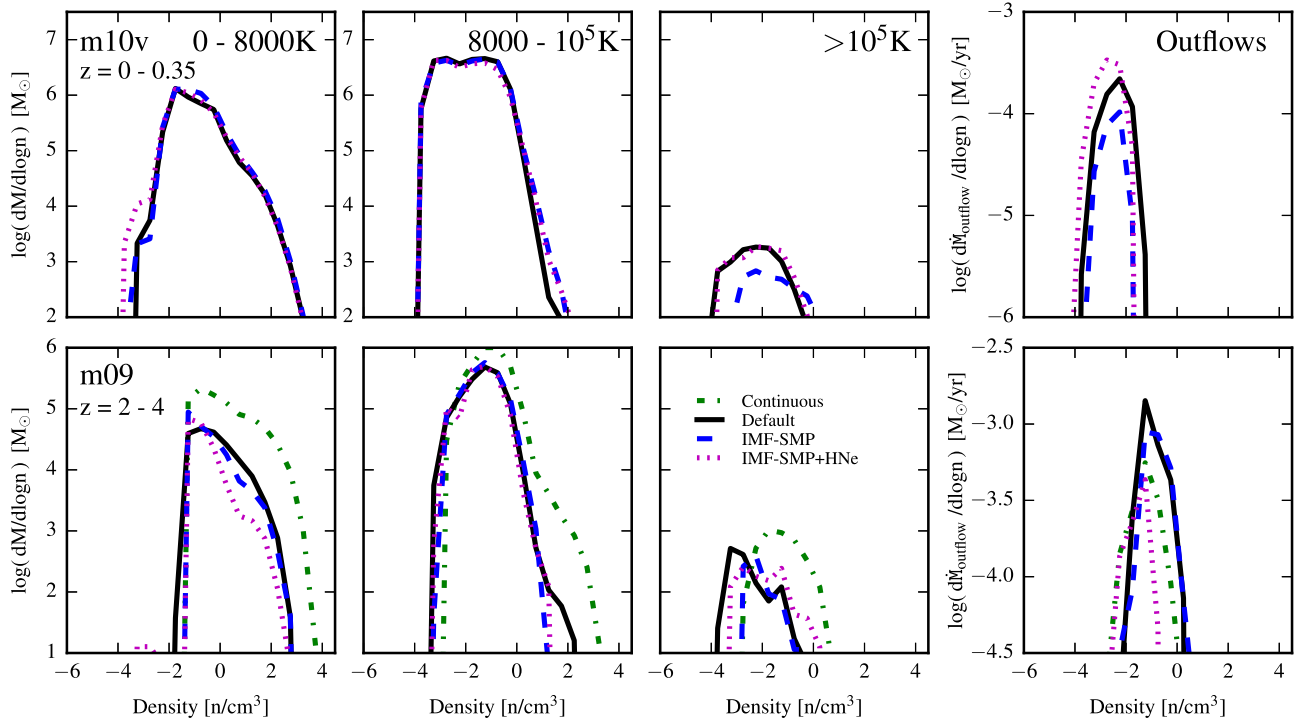


Figure 3. Density distributions of outflows and gas in different phases as in Fig. 2 but for m10v and m09. **Top Row:** ‘IMF-SMP+HNe’ run of m10v, from the time of the HNe ($z = 0.31$) to $z = 0$. **Bottom Row:** m09 from $z = 4$ to $z = 2$. The accretion rate of the ‘Continuous’ run is higher and therefore generates more cold and warm gas. HNe and IMF Sampling do not have large effects in these cases.

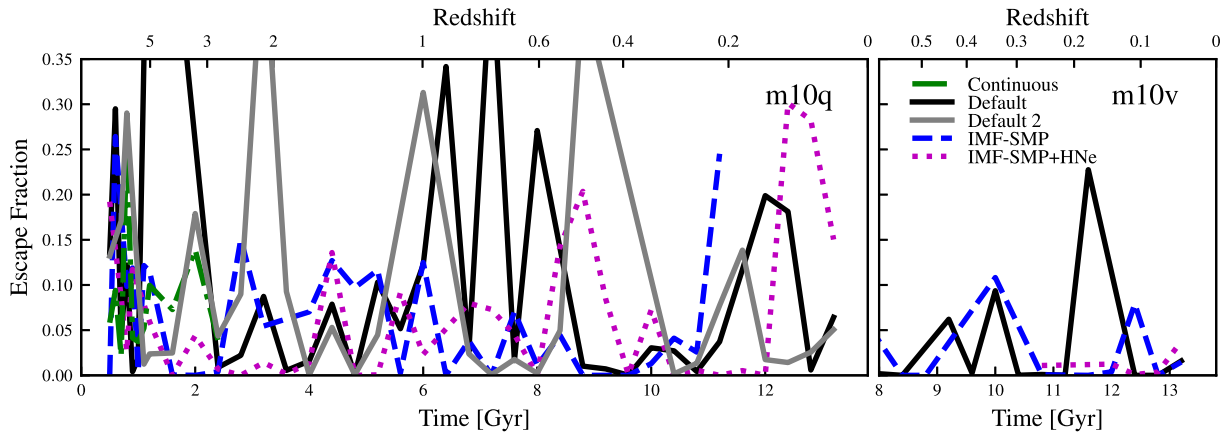


Figure 4. Photon escape fractions ($Q_{\text{esc}}/Q_{\text{int}}$) for the m10q and m10v cases. No systematic effect from IMF Sampling, SNe discretization, or HNe is observed.

is probably modest if SNe are the dominant feedback mechanism, which is often the case in dwarfs such as m10q, m10v and m09.

We note that our simulations marginally resolve the Sedov–Taylor phase of individual supernova remnants. A single SN remnant cools when it has swept out a mass $\sim 2500 f(Z)^3 M_{\odot} (n/\text{cm}^{-3})^{-2/7} (E_{\text{SN}}/10^{51} \text{ erg})^{6/7}$ of gas (where $f(Z) \sim 2$ at $Z \sim 0.01 Z_{\odot}$, owing to less-efficient cooling at low metallicities; see discussion in Hopkins et al. 2018a). So at $n \sim 1 \text{ cm}^{-3}$ and our fiducial mass resolution of $250 M_{\odot}$, this equates to ~ 80 resolution elements. ‘Pre-processing’ from other (included) stellar feedback channels (e.g. stellar winds and photoionized gas pressure) also leads to SNe preferentially exploding in lower density environments, which are marginally better resolved given the $n^{-2/7}$ dependence above (Hopkins et al. 2014; Muratov et al. 2015). Al-

though many authors have shown that underresolving SNe can make them less effective at driving outflows (Walch & Naab 2015; Forbes et al. 2016; Hu et al. 2016; Naab & Ostriker 2017), our numerical SNe coupling scheme (which explicitly accounts for un-resolved Sedov–Taylor phases before coupling) is designed specifically to handle this intermediate-resolution case and gives results as close to converged as possible. This is studied and demonstrated in detail in Hopkins et al. (2018a), for both individual SNe remnant simulations and cosmological simulations (including our m10q model here), with resolution reaching $< 1 M_{\odot}$. We explicitly show there that our $250 M_{\odot}$ runs are well converged with these much high-resolution runs in terms of bulk galaxy properties (stellar and gas masses, star formation histories, sizes). We find consistent results in our own resolution study in Appendix A.

4.2 Ineffective HNe feedback

By construction, in m10q and m10v, the *total* injected HNe energy in the simulation period is sub-dominant at ~ 10 per cent of the integrated SNe energy. In the m09 run, the energy injected by the HN is comparable to total energy injected by SNe throughout the simulation because the galaxy has so few stars.

However, just one HN is equivalent to 100 overlapping regular SNe. As such, we see a single HN can eject a large fraction of the core ISM in these low-mass dwarfs and successfully suppress star formation for ~ 1 Gyr. Eventually, the gas recycles and begins the next cycle of star formation - it is worth noting that even $\sim 10^{53}$ erg can only accelerate $\lesssim 10^6 M_{\odot}$ of gas to speeds of order the escape velocity in these systems. However, in our simulations, the star formation in such low-mass dwarfs is highly bursty and highly concentrated in some time intervals. In m10q or m10v, $\gtrsim 10^4 M_{\odot}$ stars can form in certain 100-Myr periods. In m09, although only $\sim 10^4 M_{\odot}$ form in the simulation, roughly half of that forms in the largest star burst. As a result, although HNe are very extreme versions of SNe, ~ 100 overlapping SNe do happen in the simulations occasionally and have similar effects. Therefore, including HNe in the simulations does not appreciably alter galaxy evolution, in a statistical sense, compared to 'normal' clustered and bursty star formation.

5 CONCLUSIONS

In this study, we have investigated the effects of various discrete processes in stellar feedback, including SNe, HNe, and IMF sampling on the formation and evolution of dwarf galaxies with stellar masses in the range of $\sim 10^4 - 3 \times 10^6 M_{\odot}$. We summarize our conclusions next.

(i) Discretizing SNe injection is crucial. Treating SNe as continuous energy/momentum sources with time-averaged rates (instead of individual events) smears the energy in time and space, which allows it to radiate away far too efficiently. This severely exacerbates the so-called 'overcooling problem'. As a result, feedback is effectively weaker, making galaxies accrete more gas and form orders of magnitude more stars.

(ii) Given the purely stochastic simulation variations between m10q 'Default' and 'Default 2' runs, the effects of IMF sampling are not obvious. IMF sampling also has no obvious effect on the smaller and burstier galaxies (m10v or m09).

(iii) HNe and IMF sampling effects as approximated here do not systematically affect the photon escape fraction at an appreciable level in our analysis.

(iv) The effects of HNe are not obvious in the investigated cases. While dramatic as individual events when they occur and capable of ejecting gas and shutting down SF temporarily (for up to ~ 1 Gyr) in ultra-faint dwarfs, they resemble overlapping SNe from star clusters so do not qualitatively change galaxy evolution in an aggregate, statistical sense. Since the ISM gas ejected by HNe is mostly recycled after ~ 1 Gyr, it should be possible to observe HNe yields in next-generation stars in faint dwarfs.

We caution that the toy model here for IMF sampling only scales feedback strength with some 'O-star number'. More accurately, one should draw a mass spectrum from the IMF, and some properties (e.g. photoionization) will be more strongly sensitive to the most massive stars (Hu et al. 2017). Of course, these will also produce distinct yields when they explode (Hu et al. 2017). Moreover, HNe should have different enrichment properties. HNe rate is also con-

nected with the IMF, which could be redshift dependent. At high redshift, the HNe event rate can be 10 times higher than in low redshift (Cooke et al. 2012), which can possibly further change the halo mass at reionization and therefore also the post-reionization accretion. Modjaz et al. (2008) and Modjaz et al. (2011) also showed that HNe are more likely to happen in low-metallicity environments. These aspects are left for future work. Besides the discreteness in feedback processes investigated in the current study, there are other processes that could be interesting and can be crucial in galaxy evolution. For instance, SNe injection should also affect the cosmic-ray (CR) energy budget, which is not included in the current feedback model but can have a large effect on ISM properties and outflows (Girichidis et al. 2016a; Simpson et al. 2016; Ruzsokowski, Yang & Reynolds 2017a; Ruzsokowski, Yang & Zweibel 2017b). Detailed examination of these processes will also be left for future work.

ACKNOWLEDGEMENTS

Support for PFH was provided by Alfred P. Sloan Research Fellowship, NASA ATP Grant NNX14AH35G, and NSF Collaborative Research Grant #1411920 and CAREER grant #1455342. The Flatiron Institute is supported by the Simons Foundation. Numerical calculations were run on the Caltech compute cluster 'Zwicky' (NSF MRI award #PHY-0960291) and allocation TG-AST130039 granted by the Extreme Science and Engineering Discovery Environment (XSEDE) supported by the NSF. D. Kereš was supported by NSF grants AST-1412153 and AST-1715101 and the Cottrell Scholar Award from the Research Corporation for Science Advancement. CAFG was supported by NSF through grants AST-1412836, AST-1517491, AST-1715216, and CAREER award AST-1652522, and by NASA through grant NNX15AB22G. MBK acknowledges support from NSF grant AST-1517226 and from NASA grants NNX17AG29G and *HST*-AR-13888, *HST*-GO-14191, *HST*-AR-14282, and *HST*-AR-14554 from the Space Telescope Science Institute, which is operated by AURA, Inc., under NASA contract NAS5-26555. M. Orr is supported by the NSF GFRP under grant No 1144469.

REFERENCES

- Agertz O., Kravtsov A. V., 2015, *ApJ*, 824, 79
 Anders E., Grevesse N., 1989, *Geochim. Cosmochim. Acta*, 53, 197
 Anglés-Alcázar D., Faucher-Giguère C.-A., Kereš D., Hopkins P. F., Quataert E., Murray N., 2017, *MNRAS*, 470, 4698
 Bryan G. L., Norman M. L., 1998, *ApJ*, 495, 80
 Ceverino D., Klypin A., 2009, *ApJ*, 695, 292
 Cole S., Lacey C. G., Baugh C. M., Frenk C. S., 2000, *MNRAS*, 319, 168
 Cooke J. et al., 2012, *Nature*, 491, 228
 da Silva R. L., Fumagalli M., Krumholz M., 2012, *ApJ*, 745, 145
 Dwek E., 1998, *ApJ*, 501, 643
 El-Badry K., Wetzel A., Geha M., Hopkins P. F., Kereš D., Chan T. K., Faucher-Giguère C.-A., 2016, *ApJ*, 820, 131
 Faucher-Giguère C.-A., 2018, *MNRAS*, 473, 3717
 Faucher-Giguère C.-A., Lidz A., Zaldarriaga M., Hernquist L., 2009, *ApJ*, 703, 1416
 Faucher-Giguère C.-A., Hopkins P. F., Kereš D., Muratov A. L., Quataert E., Murray N., 2015, *MNRAS*, 449, 987
 Faucher-Giguère C.-A., Feldmann R., Quataert E., Kereš D., Hopkins P. F., Murray N., 2016, *MNRAS*, 461, L32
 Fielding D., Quataert E., Martizzi D., Faucher-Giguère C.-A., 2017, *MNRAS*, 470, L39
 Fitts A. et al., 2017, *MNRAS*, 471, 3547
 Forbes J. C., Krumholz M. R., Goldbaum N. J., Dekel A., 2016, *Nature*, 535, 523

Fumagalli M., Prochaska J. X., Kasen D., Dekel A., Ceverino D., Primack J. R., 2011, *MNRAS*, 418, 1796

Gal-Yam A., 2012, *Science*, 337, 927

Girichidis P. et al., 2016a, *ApJ*, 816, L19

Girichidis P. et al., 2016b, *MNRAS*, 456, 3432

Governato F., Willman B., Mayer L., Brooks A., Stinson G., Valenzuela O., Wadsley J., Quinn T., 2007, *MNRAS*, 374, 1479

Guetta D., Della Valle M., 2007, *ApJ*, 657, L73

Hafen Z. et al., 2017, *MNRAS*, 469, 2292

Hansen B. M. S., 1999, *ApJ*, 512, L117

Hensler G., Steyrlleithner P., Recchi S., 2017, in Gil de Paz A., Knapen J.H., Lee J.C. in *Formation and Evolution of Galaxy Outskirts*, Proc. IAU Symp. 11, 321, p. 99

Hopkins P. F., 2015, *MNRAS*, 450, 53

Hopkins P. F., Quataert E., Murray N., 2011, *MNRAS*, 417, 950

Hopkins P. F., Quataert E., Murray N., 2012a, *MNRAS*, 421, 3522

Hopkins P. F., Quataert E., Murray N., 2012b, *MNRAS*, 421, 3522

Hopkins P. F., Quataert E., Murray N., 2012c, *MNRAS*, 421, 3488

Hopkins P. F., Cox T. J., Hernquist L., Narayanan D., Hayward C. C., Murray N., 2013a, *MNRAS*, 430, 1901

Hopkins P. F., Kereš D., Murray N., Hernquist L., Narayanan D., Hayward C. C., 2013b, *MNRAS*, 433, 78

Hopkins P. F., Narayanan D., Murray N., 2013c, *MNRAS*, 432, 2647

Hopkins P. F., Kereš D., Oñorbe J., Faucher-Giguère C.-A., Quataert E., Murray N., Bullock J. S., 2014, *MNRAS*, 445, 581

Hopkins P. F. et al., 2018a, *MNRAS*, 477, 1578

Hopkins P. F. et al., 2018b, *MNRAS*, e-print (arXiv:1702.06148)

Hu C.-Y., Naab T., Walch S., Glover S. C. O., Clark P. C., 2015, *MNRAS*, 458, 3528

Hu C.-Y., Naab T., Walch S., Glover S. C. O., Clark P. C., 2016, *MNRAS*, 458, 3528

Hu C.-Y., Naab T., Glover S. C. O., Walch S., Clark P. C., 2017, *MNRAS*, 471, 2151

Jefferies J. T., 1969, *Spectral Line Formation*, Blaisdell

Kasen D., Thomas R. C., Nugent P., 2006, *ApJ*, 651, 366

Katz N., Weinberg D. H., Hernquist L., 1996, *ApJS*, 105, 19

Kereš D., Katz N., Davé R., Fardal M., Weinberg D. H., 2009, *MNRAS*, 396, 2332

Kim C.-G., Ostriker E. C., 2015, *ApJ*, 802, 99

Kim C.-G., Ostriker E. C., 2017, *ApJ*, 846, 133

Kim C.-G., Ostriker E. C., Kim W.-T., 2013, *ApJ*, 776, 1

Kim C.-G., Ostriker E. C., Kim W.-T., 2014, *ApJ*, 786, 64

Kim C.-G., Ostriker E. C., Raileanu R., 2017, *ApJ*, 834, 25

Kroupa P., 2002, *Science*, 295, 82

Krumholz M. R., Fumagalli M., da Silva R. L., Rendahl T., Parra J., 2015, *MNRAS*, 452, 1447

Leitherer C. et al., 1999, *ApJS*, 123, 3

Ma X., Hopkins P. F., Faucher-Giguère C.-A., Zolman N., Muratov A. L., Kereš D., Quataert E., 2015a, *MNRAS*, 456, 2140

Ma X., Kasen D., Hopkins P. F., Faucher-Giguère C.-A., Quataert E., Kereš D., Murray N., 2015b, *MNRAS*, 453, 960

Ma X., Hopkins P. F., Kasen D., Quataert E., Faucher-Giguère C.-A., Kereš D., Murray N., Strom A., 2016, *MNRAS*, 459, 3614

Martizzi D., Faucher-Giguère C.-A., Quataert E., 2015, *MNRAS*, 450, 504

Martizzi D., Fielding D., Faucher-Giguère C.-A., Quataert E., 2016, *MNRAS*, 459, 2311

Modjaz M. et al., 2008, *AJ*, 135, 1136

Modjaz M., Kewley L., Bloom J. S., Filippenko A. V., Perley D., Silverman J. M., 2011, *ApJ*, 731, L4

Muratov A. L., Kereš D., Faucher-Giguère C.-A., Hopkins P. F., Quataert E., Murray N., 2015, *MNRAS*, 454, 2691

Muratov A. L. et al., 2017, *MNRAS*, 468, 4170

Naab T., Ostriker J. P., 2017, *ARA&A*, 55, 59

Nomoto K., Tominaga N., Umeda H., Maeda K., Ohkubo T., Deng J., Mazzali P. A., 2005, Humphreys R., Stanek K., in , ed., *The Fate of the Most Massive Stars*, ASP Conference Series, Vol. 332. Astronomical Society of the Pacific, San Francisco, p. 384

Orr M. et al., 2017, *MNRAS*, 478, 3653

Podsiadlowski P., Mazzali P. A., Nomoto K., Lazzati D., Cappellaro E., 2004, *ApJ*, 607, L17

Richings A. J., Schaye J., 2016, *MNRAS*, 458, 270

Ruszkowski M., Yang H.-Y. K., Reynolds C. S., 2017a, *ApJ*, 844, 13

Ruszkowski M., Yang H.-Y. K., Zweibel E., 2017b, *ApJ*, 834, 208

Simpson C. M., Pakmor R., Marinacci F., Pfrommer C., Springel V., Glover S. C. O., Clark P. C., Smith R. J., 2016, *ApJ*, 827, L29

Soderberg A. M. et al., 2006, *Nature*, 442, 1014

Somerville R. S., Primack J. R., 1999, *MNRAS*, 310, 1087

Sparre M., Hayward C. C., Feldmann R., Faucher-Giguère C.-A., Muratov A. L., Kereš D., Hopkins P. F., 2017, *MNRAS*, 466, 88

Springel V., Hernquist L., 2003, *MNRAS*, 339, 289

Stanway E. R., Eldridge J. J., Becker G. D., 2016, *MNRAS*, 456, 485

Uhlig M., Pfrommer C., Sharma M., Nath B. B., Enßlin T. A., Springel V., 2012, *MNRAS*, 423, 2374

Verner D. A., Ferland G. J., 1996, *ApJS*, 103, 467

Verner D. A., Ferland G. J., Korista K. T., Yakovlev D. G., 1996, *ApJ*, 465, 487

Walch S., Naab T., 2015, *MNRAS*, 451, 2757

APPENDIX A: RESOLUTION STUDY

The resolution-dependence and convergence properties of our simulations (as well as other numerical properties, e.g. sensitivity to the numerical hydrodynamic methods) – including specifically the three dwarf galaxies studied here – have been studied extensively over several orders of magnitude in resolution (involving many additional galaxy properties) in Hopkins et al. (2017b,). We refer to those papers for much more extensive analysis.

Table A1. Particle resolutions used in our convergence tests for the default m10q run.

Resolution	Physics	$m_{i,1000}$	$m_{d,1000}$
MR	Default	0.25	1.3
MR	Default	0.25	1.3
MR	IMF-SMP	0.25	1.3
HR	IMF-SMP	0.03	0.16

Notes: (1) Resolution name. MR: Medium resolution. HR: High resolution. (2) Physics: The variants are described in Section 2. (3) $m_{i,1000}$: Baryonic (star and gas) mass resolution in units of 1000 M_{\odot} . (4) $m_{d,1000}$: Dark matter mass resolution in units of 1000 M_{\odot} .

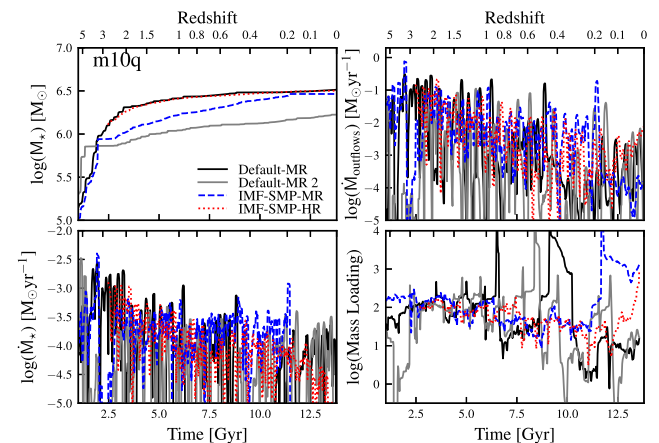


Figure A1. Comparison of the total stellar mass (*upper left*), SFR (*bottom left*), outflow rate (*upper right*), and outflow mass loading (*bottom right*). The differences between the 'IMF-SMP' HR and MR runs are within the stochastic range characterized by the two 'Default' runs.

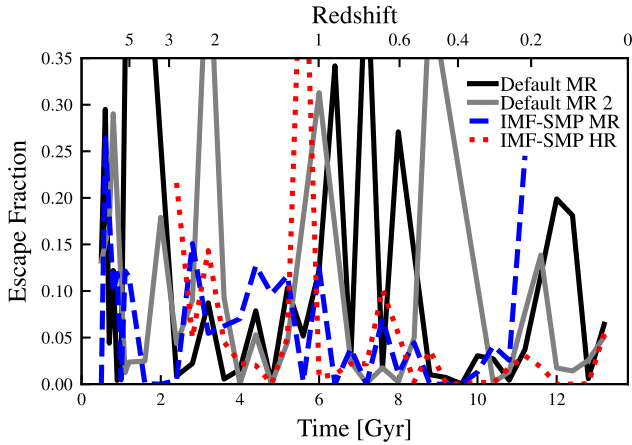


Figure A2. Comparison of the photon escape fractions. The ‘IMF-SMP’ runs with different resolutions have similar photon escape fractions.

However, we have briefly considered resolution studies of our ‘new physics’ IMF-SMP runs, for each of our haloes. The con-

clusions are identical, so we focus on m10q here and compare a run with ~ 10 times higher particle mass – i.e. $30 M_{\odot}$ resolution (we have also varied the resolution by a factor of ~ 10 towards lower resolution and again find consistent results, but these are less interesting).

The run list is included in Table A1. The MR runs match the resolution of the corresponding m10q runs in the main text. The two ‘Default’ runs from the main text are also included, indicating the range of stochastic variations of different physical quantities.

Fig. A1 shows the total stellar mass, star formation rate, outflow rate, and outflow mass loading of the ‘IMF-SMP’ runs with different resolutions. Fig. A2 shows the escape fractions. Fig. A3 shows the masses of gas in different phases, including cold-neutral, warm-ionized, and hot, and in outflows as a function of density at different redshifts. For all plotted quantities, the difference between the ‘IMF-SMP’ HR and MR runs are within the stochastic range characterized by the two ‘Default’ runs. This indicates that our results are reasonably converged at the fiducial resolution.

This higher resolution run as well as similar runs at ultra-high resolution ($\sim 10\text{--}50 M_{\odot}$ mass resolution) will be studied systematically in future work (Wheeler et al., in preparation).

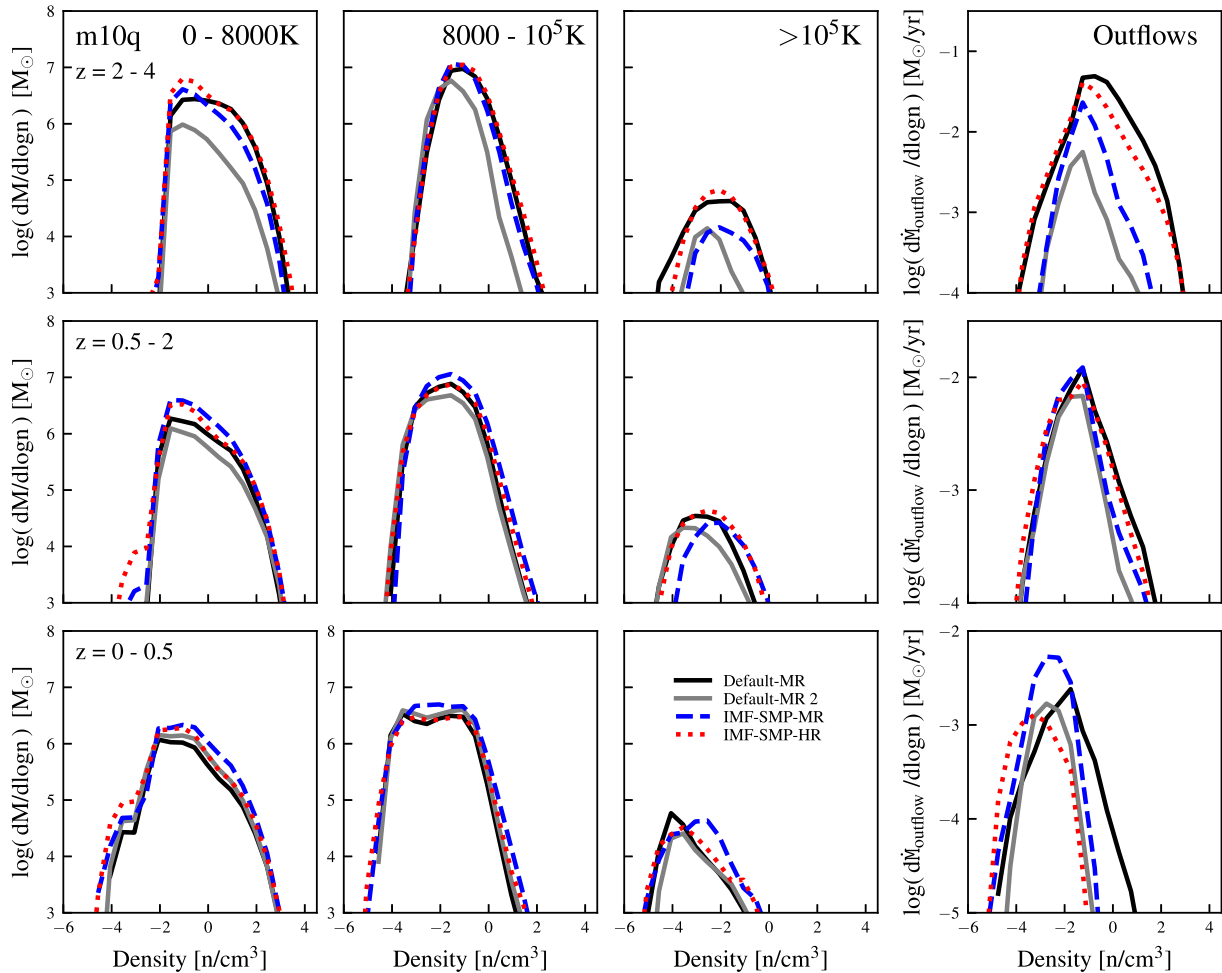


Figure A3. Gas density distributions for m10q. Rows show the properties at different redshifts; columns show different phases, including cold-neutral (left), warm-ionized (middle left), hot (middle right), and outflows (right). The differences between the ‘IMF-SMP’ HR and MR runs are within the stochastic range characterized by the two ‘Default’ runs.

This paper has been typeset from a \LaTeX file prepared by the author.